# High-Speed Microfabricated Silicon Turbomachinery and Fluid Film Bearings

Luc G. Fréchette, *Member, IEEE, Member, ASME*, Stuart A. Jacobson, *Member, ASME*,
Kenneth S. Breuer, *Senior Member, ASME*, Fredric F. Ehrich, *Fellow, ASME*, Reza Ghodssi, *Member, IEEE*,
Ravi Khanna, *Member, IEEE*, Chee Wei Wong, *Member, IEEE, Member, ASME*,
Xin Zhang, *Member, IEEE, Member, ASME*, Martin A. Schmidt, *Fellow, IEEE*, and Alan H. Epstein, *Member, ASME*

*Abstract*—A single-crystal silicon micromachined air turbine supported on gas-lubricated bearings has been operated in a controlled and sustained manner at rotational speeds greater than 1 million revolutions per minute, with mechanical power levels approaching 5 W. The device is formed from a fusion bonded stack of five silicon wafers individually patterned on both sides using deep reactive ion etching (DRIE). It consists of a single stage radial inflow turbine on a 4.2-mm diameter rotor that is supported on externally pressurized hydrostatic journal and thrust bearings. This paper presents the design, fabrication, and testing of the first microfabricated rotors to operate at circumferential tip speeds up to 300 m/s, on the order of conventional high performance turbomachinery. Successful operation of this device motivates the use of silicon micromachined high-speed rotating machinery for power microelectromechanical systems (MEMS) applications such as portable energy conversion, micropropulsion, and microfluidic pumping and cooling. **[1161]**

*Index Terms*—Bearings, lubrication, microengines, microturbine, power MEMS, turbomachinery.

## I. INTRODUCTION

ROTATING machinery is commonly used in our society for a wide range of energy conversion applications, such as electric power generation, propulsion, cooling and ventilation. Components such as motors and turbines convert electrical or fluid power to mechanical power as the product of shaft torque and rotation rate. To achieve high specific power (defined as the device power per unit mass) high peripheral speeds are desirable. For example, gas turbine engines operate at supersonic tip speeds of hundreds of meters per second and deliver on the order of megawatts per ton, or watts per gram, of propulsive or electric power. Such gas turbines burning hydrocarbon fuels have high power and energy densities, suggesting they could be appropriate for small scale or portable power applications if they could be scaled down. For instance, portable electronic devices, micro air vehicle propulsion, and coolers for electronics and people require a lightweight power source that supplies on the order of 10–100 W over many hours. Today's best batteries poorly serve these types of applications and impose significant constraints on their functionality and feasibility. To match this power level, high-speed turbomachinery would need to be miniaturized to millimeter-scale blades, imposing micrometer-scale tolerances to obtain sufficient performance levels. These small scales, in combination with the stringent mechanical strength requirements for high-speed machinery, have made fabrication of microengines using traditional manufacturing techniques prohibitive.

Microfabrication and microelectromechanical systems (MEMS) technology offer an attractive alternative to traditional methods for building microengines, although yet to be demonstrated. Previous microfabricated rotating machines have mostly been designed for low force actuation instead of power conversion, hence typically operated at less than 1 m/s of peripheral (tangential) speed, which is two orders of magnitudes less than that required for practical energy conversion applications. Examples include surface micromachined electrostatic micromotors [1], [2], high aspect ratio magnetic and electrostatic micromotors based on LIGA or other electrode-position techniques [3], [4], and surface micromachined gear trains actuated by electrostatic linear comb drives [5]. Rotors are typically supported by solid contact on a central post, and therefore stiction and wear have been important considerations [6], although lessened by the low-peripheral speed that these devices have operated.

An on-going effort at the Massachusetts Institute of Technology aims to develop microscale high-speed rotating machinery and microheat engine technology using silicon micromachining and other MEMS fabrication processes [7]. It was proposed that lithographic patterning, deep-reactive ion etching (DRIE), and wafer bonding could be used to fabricate integrated single-crystal silicon or refractory ceramic micro energy conversion systems with high power densities. Initial work has mostly focused on system level design and core component development for power MEMS devices such as a micro gas turbine engine [8], a micro rocket engine [9], and a microcompressor [10]. Previous work has established
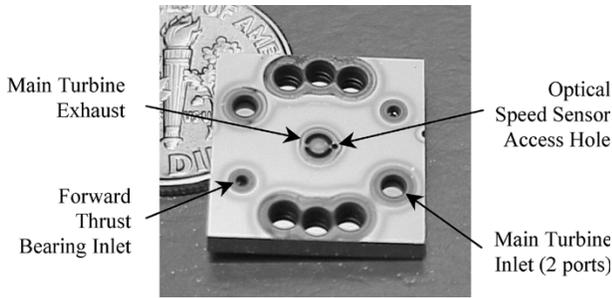
Fig. 1. Microturbine-driven bearing rig die, consisting of a diced five-wafer bonded stack (15 mm × 15 mm), which encloses a free silicon rotor.

technical and scientific foundations for microscale combustion [11], [12], gas lubricated bearings [13], [14], turbomachinery [15], [16], electromechanical machinery [17], [18], and device microfabrication [19], [20]. The work presented herein focuses on the successful experimental demonstration of two central technologies for rotary microengines: fluid film microbearings and microturbomachinery.

In the current approach, the high-speed rotor is etched from a bulk silicon substrate, taking advantage of the high strength-to-density ratio of single-crystal silicon and the low flaw density of commercial semiconductor wafers. This material choice provides unique capabilities to withstand the stress levels induced by the centrifugal forces at high tip speeds. In order to minimize the resistance to rotation and prevent wear that would result from solid contact, the rotor is supported by gas-lubricated, fluid-film bearings. Microturbomachinery is used as a drive source for high-power density fluid-to-mechanical energy conversion, similar to many large-scale power generation systems.

To demonstrate this approach and develop the core technology, a microturbine-driven bearing rig was developed, and will be the focus of this paper. This device, which is a subset of a complete micro gas turbine engine, consists of a pressure-driven microturbine rotor supported on gas-lubricated bearings, integrated in a bonded stack of five silicon wafers. This paper presents the design, fabrication, and operational achievements of this high-speed rotating microturbine, for which initial development efforts and results were first presented by Lin *et al.* [19] and Fréchette *et al.* [21]. Section II presents the device design and underlying operating principles. Section III summarizes the fabrication process and also includes a discussion of the main fabrication challenges. Section IV presents the experimental procedures and test results, followed by discussions and conclusions in Sections V and VI, respectively.

## II. DEVICE DESIGN AND DESCRIPTION

### A. Overall Configuration

The microturbine device, shown in Figs. 1 and 2, consists of a 4.2-mm-diameter rotor enclosed in a fusion-bonded stack of five aligned, through-etched silicon wafers. The rotor is a planar disk with radial turbine blades on its front side. Pressurized air enters the device near the outer edge, flows radially inward through the turbine, and exhausts axially near the center of the device. A gas journal bearing on the periphery of the rotor supports radial motion, while a pair of gas thrust bearings along the rotor

centerline supports axial motion. In this device, torque delivered by the turbine simply counteracts the viscous friction on the rotor, since the objective is to experimentally develop the turbine and air bearings. A load could be integrated with the rotor, such as an electric generator, a compressor, or a pump, as proposed by Epstein *et al.* [7]. The following sections describe the design and operating principles of the main components.

### B. Microturbine

The microturbine provides torque on the rotor by converting fluid power to mechanical power. The curved stator vanes, shown in Fig. 3, turn the inward flow away from purely radial, imparting angular momentum as it accelerates. The turbine rotor blades turn the flow back toward the radial direction, extracting angular momentum in the process and producing torque on the rotor. The power transferred to the rotor is the product of this torque and the rotor's angular rotation rate. For this application, the turbine must only provide enough power to overcome the viscous drag on the rotor, typically induced in the bearings. To simulate the load encountered in a complete energy conversion system, such as that from an electric generator that would be integrated with the rotor for electric power generation [7], the viscous drag was increased by reducing the clearance over the backside of the rotor. For the current configuration, the total viscous power is approximately 13 W at a circumferential tip speed of 500 m/s and is proportional to the square of the rotation rate. The turbine used herein was designed to provide 60 W of mechanical power for an inlet pressure of 8 atm and inlet temperatures of 600 K. While viscous drag can become predominant in microsystems due to the small length scale [16], it remains a fraction of the power predicted for high-speed turbomachinery.

The blade shapes were designed using MISES, a two-dimensional (2-D) computational fluid dynamics code developed at MIT [22]. MISES is an Euler solver coupled to an integral boundary layer formulation. Fig. 4 shows a portion of the turbine, along with velocity triangles computed in MISES at a design rotation rate of 250 000 rad/s. The velocity triangles indicate the velocity vectors in an absolute (nonrotating) reference frame $(C)$ and a relative (rotating) reference frame $(W)$, related by the tangential rotor speed $(U = \Omega r)$. Fig. 4 also shows computed streamlines around a stator vane and a rotor blade indicating the extent of the boundary layers. Note that the exit streamlines from the stator (calculated in the absolute frame) match the direction of the absolute flow vector $C_2$ and the inlet streamlines to the turbine (calculated in the relative frame) match the direction of the relative flow vector $W_2$. Under the assumption that little swirl in the turbine exhaust could be recovered, the turbine was designed to have very little swirl in the exit absolute flow $(C_3)$. The turbine configuration and the flow conditions predicted with MISES at the design speed are summarized in Table I. The actual flow through the turbine is expected to be three-dimensional (3-D), mainly due to boundary layer growth on the end-walls. However, because the turbine flow is expanding, the 3-D effects are not expected to be substantial [15].

The particular challenge in the design of microturbomachinery for MEMS results from the microfabrication constraint
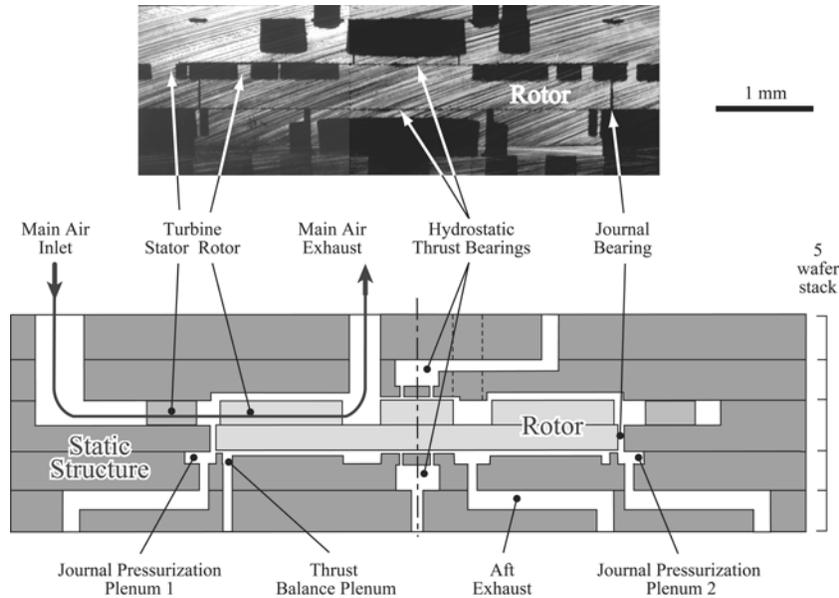
Fig. 2. Optical photograph (top) and schematic (bottom) of a cross section of the microturbine-driven bearing rig. For scale reference, the rotor is 4.2 mm in diameter.
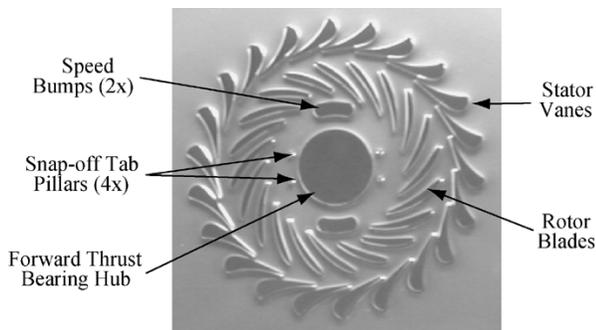


Fig. 3. Optical photograph of the 4.2-mm diameter microturbine showing the stator and rotor blades (150 $\mu$m tall), two symmetric speed bumps, and four pillars for the snap-off tabs. In this picture, the journal bearing gap remains to be etched.

TABLE I
MICROTURBINE CONFIGURATION AND DESIGN OPERATING CONDITIONS

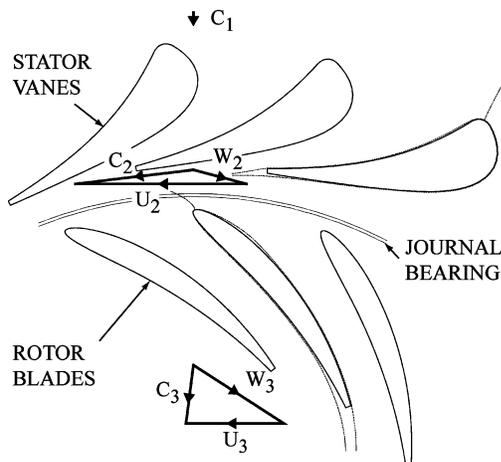|  | Stator vanes | Rotor blades |
|---|---|---|
| *Number of blades* | 22 | 20 |
| *Radial      leading edge* | 2.8 mm | 2.0 mm |
| *position    trailing edge* | 2.2 mm | 1.4 mm |
| *Rotor radius* | 2.1 mm | |
| *Blade height* | 150 microns | |
| *Design speed* | 250,000 rad/s | |
| *Design flow rate* | 0.3 g/s (15,000 sccm) | |
| *Inlet velocity* | 22 m/s (abs.) | 175 m/s (rel.) |
| *Exit velocity* | 380 m/s (abs.) | 344 m/s (rel.) |
| *Inlet flow angle* | 0° (abs.) | -75° (rel.) |
| *Exit flow angle* | 83° (abs.) | -57° (rel.) |
| *Design pressure ratio* | 5.4 | |
| *Isentropic efficiency* | 87 % (2-D MISES) | |
| *Design shaft power* | 60 W | |



Fig. 4. Velocity triangles through the microturbine computed with MISES at a design rotation rate of 250 000 rad/s. Dashed lines around a stator vane and rotor blade outline the boundary layers.

that limits the geometry to uniform blade height. A more traditional design for centrifugal turbomachinery would allow

the blade height to vary inversely with radius to compensate for the increase in circumference with radius. The resulting blade designs reflect the different strategies that a designer must use to adjust for the differences in fabrication capability.

### C. Thrust Bearings

The hydrostatic thrust bearings shown in Fig. 2 act as a pair of self-restoring axial springs that maintain the rotor between the surfaces above and below the rotor, without physical contact. Each thrust bearing consists of a circular array of restrictors that feed pressurized air to a radial thrust bearing gap separating the rotor from the stationary surface [see Fig. 5(a)]. A hydrostatic axial force results from integrating the radial film pressure distribution along the thrust bearing gap, and strongly depends on the restrictor exit pressure ($P_f$). By adjusting the pressure supplied to the forward and aft thrust bearing restrictors (in the range of 35–85 psig), the axial position of the rotor can be modified. This configuration also provides axial stiffness by automatically adjusting the film pressure to compensate for
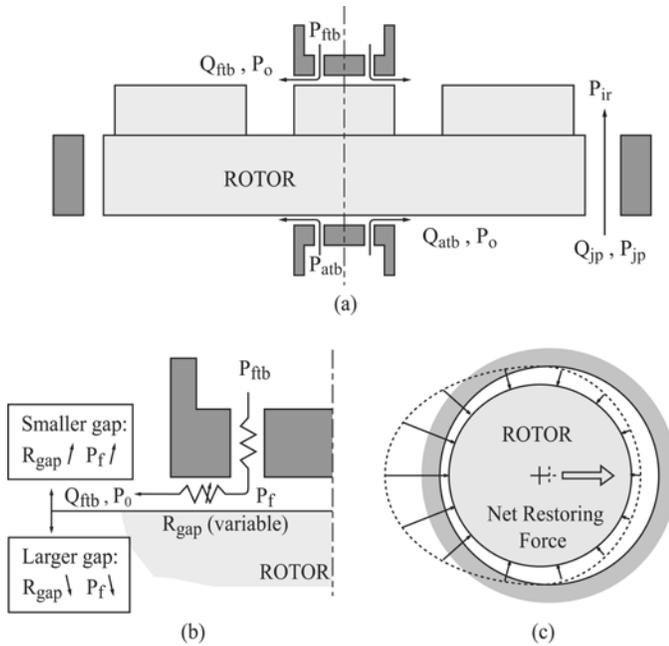
Fig. 5. Schematic of the bearing system, illustrating the operating principles of the thrust and journal bearings. (a) Rotor cross section with thrust and journal bearings. (b) Hydrostatic thrust bearing (forward side). (c) Hydrostatic journal bearing with circumferential pressure distribution (plan view).

TABLE II
HYDROSTATIC THRUST BEARING CONFIGURATION AND TYPICAL OPERATING
CONDITIONS FOR CENTERED POSITION

|  | Forward | Aft |
|---|---|---|
| *Restrictor:  number* | 14 | 18 |
| *Diameter* | 10 microns | 10 microns |
| *Location* | r=0.55 mm | r=0.75 mm |
| *Bearing outer radius* | 0.7 mm | 0.9 mm |
| *Bearing gap (nominal)* | 1.5 microns | 1.5 microns |
| *Typical supply pressures* | 35 psig | 60 psig |
| *Predicted axial stiffness* | 0.26 N/micron | |

a perturbation in axial position, even with constant feed pressures. For example, an upward perturbed motion of the rotor will reduce the radial gap height in the forward thrust bearing [see Fig. 5(b)], effectively increasing its flow resistance ($R_{gap}$). Since the overall pressure difference ($P_{ftb} - P_0$) is kept constant, the flow rate will diminish. This will result in a higher film pressure ($P_f$) due to the lower pressure drop across the restrictor ($P_{ftb} - P_f$). A higher downward pressure force will therefore be applied on the rotor. Combined with the opposite behavior of the aft thrust bearing, the net force will tend to restore the rotor to its original position, opposing the perturbation. This microfabricated hydrostatic thrust bearing configuration was demonstrated in the first generation of this device [19]. A revised geometry for improved stiffness was implemented here, with the resulting geometry described in Table II. Optimal stiffness was achieved by evenly distributing the pressure drop between the restrictors and the radial gap.

### D. Journal Bearing

A hydrostatic gas journal bearing supports the rotor in the plane of rotation. It simply consists of a circumferential gap around the rotor periphery, in which a pressurized fluid film is maintained to prevent solid contact and allow free rotation. The journal bearing is 300 $\mu$m in axial length with an average radial gap of 15 $\mu$m. This gives a bearing length ratio (defined as journal bearing length over rotor diameter) of $7 \times 10^{-2}$, which is an order of magnitude shorter than conventional bearings, and a clearance ratio (defined as journal bearing gap over rotor radius) at $7 \times 10^{-3}$, which is approximately five times larger than conventional. A pressure differential is maintained across the journal bearing, generating an axial through flow. On the front side of the rotor, the journal bearing boundary pressure is set by the stator exit/rotor inlet pressure, referred to as the interrow pressure ($P_{ir}$). On the back side of the rotor, the journal bearing opens into a large plenum whose pressure can be set externally. The current implementation splits the back side plenum into two symmetric journal pressurization plenums, as shown in Fig. 2, although for current testing these two plenums are set to the same pressure ($P_{jp1} = P_{jp2} = P_{jp}$).

An axial flow through the gap is forced by maintaining the journal pressurization plenum pressure higher than the interrow pressure ($\Delta P = P_{jp} - P_{ir} > 0$). A local radial force on the rotor will result from the integrated axial pressure distribution along the rotor side wall. At significantly large Reynolds numbers ($Re > 10$), this pressure profile depends on losses incurred when entering the bearing gap and with the development of boundary layers along the gap. Since these losses can vary with the local gap width and flow rate, so will the local radial hydrostatic force. For example, when the rotor moves off center, the journal bearing width is smaller on one side than on the other. Axial flow along the smaller gap will rapidly reach fully developed conditions and exhibit less inlet pressure losses compared to flow along the larger gap. Higher entry losses in the larger gap will reduce the static pressure and consequently lower the local pressure force acting on that portion of the circumference. When the pressure is integrated across and around the journal bearing, the resultant in-plane force on the rotor is a restoring one, in the direction opposing the initial displacement [Fig. 5(c)]. This configuration therefore provides a net restoring force to in-plane perturbations, performing like a damped spring in a lumped-element analogy. This hydrostatic bearing scheme was experimentally demonstrated by Orr [14] on a 26× scaled-up bearing rig of similar geometry, and the principle has also been found in pump seals, referred to as the Lomakin effect [23]. Further details on the hydrostatic journal bearing operation can be found elsewhere [14], [24].

In addition to the journal pressurization plenums, there is a circumferential plenum on the back side of the device, referred to in Fig. 2 as the thrust balance plenum. While there is no stiffness (i.e., change of force with displacement) associated with this plenum, it is used to set the static pressure over most of the rotor aft side and help cancel axial forces on the rotor. The thrust balance plenum can be coupled to pressures elsewhere in the system, allowing the operator to compensate for axial loads that develop on the rotor as the pressure across the turbine is increased. In order to deliver pressurized air to the various micron-scale bearing components and to the turbine, internal piping was integrated within the multiwafer device, as described in the following section.
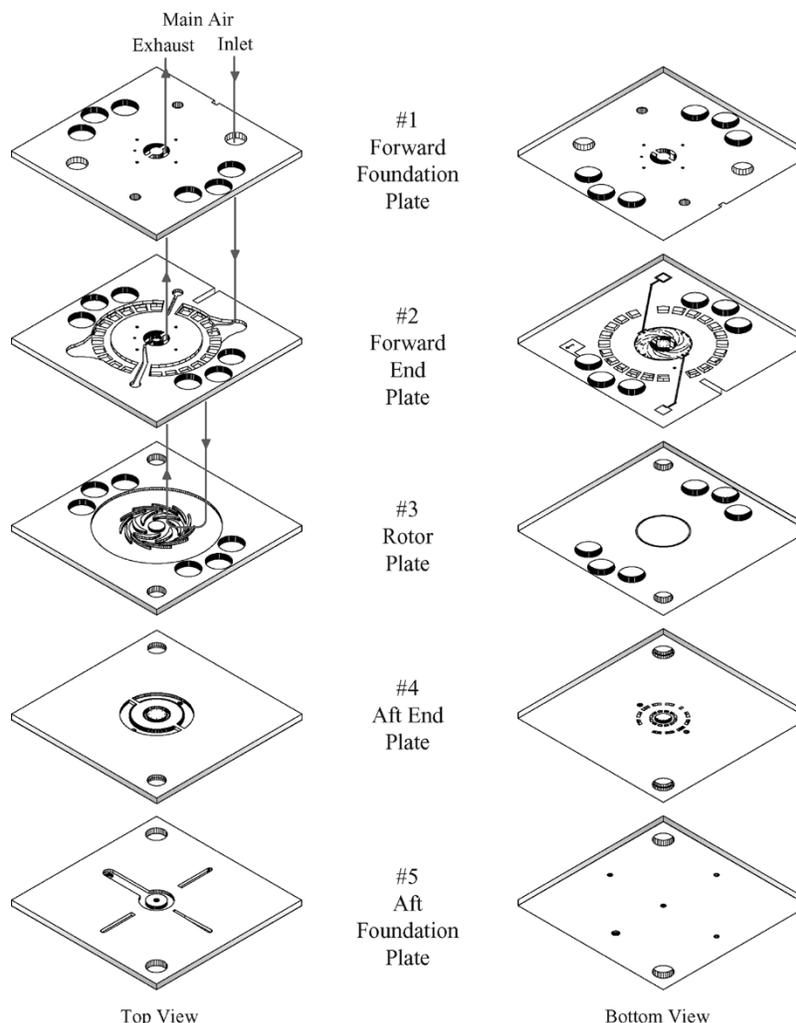
Fig. 6. Exploded top and bottom views of the five wafer stack device. The completed die is 15 mm per side and 2.3 mm thick.

## III. FABRICATION

This section summarizes the fabrication sequence to create the microturbine device and comments on some of the key processing challenges, such as high-aspect ratio DRIE, multiwafer aligned fusion bonding, and an approach to encapsulate and release a rotor in a complete chip without part handling.

### A. Process Flow

The process flow is based on DRIE and aligned fusion bonding of silicon wafers, as first presented by Lin *et al.* [19] and previously reported by Fréchette *et al.* [21]. An exploded view of the five-wafer stack device is shown in Fig. 6. The center wafer (#3) is referred to as the rotor plate and includes the most critical component of the device, i.e., the single-crystal silicon rotor. Adjacent wafers (end plates #2 and #4) form the stationary surfaces of the thrust bearings and fluid piping. The outer most wafers (foundation plates #1 and #5) provide external fluidic ports that supply pressurized gases to the turbine and the bearing system, as well as through holes to permit direct optical viewing of the enclosed rotor. The process flow is illustrated in Fig. 7. First, the end plates (wafers #2 and #4) receive two shallow silicon etches on their side facing the rotor to create thrust bearing gaps (1.5 $\mu$m) and clearances for the

turbine blades (12.5 $\mu$m on wafer #2) and the rotor back side (8 $\mu$m on wafer #4). All wafers are then deep etched partway through their thickness, except for wafer #1, which is etched completely through from its bottom side. Wafers #2, #4, and #5 are patterned on the opposite side using infrared alignment and then deep etched until through-flow channels are created.

The five wafer stack is then completed in two bonding steps and one etch step. First, the rotor plate (wafer #3) is aligned fusion bonded to the forward end plate (wafer #2), creating a physical link between the center of the rotor and the forward end plate (wafer #2). A narrow circular trench is then etched from the aft side of the rotor plate (wafer #3) to define the journal bearing gap, and consequently the rotor. As will be discussed later, the rotor remains temporarily attached to the forward end plate (wafer #2) until the device is completed. The third step then consists of align fusion bonding the remaining plates (wafers #1, #4, and #5) to the #2-#3 wafer pair. The five wafer stack is then diced to separate the individual devices shown in Fig. 1. Each rotor is therefore completely enclosed by a monolithic silicon structure, from which it needs to be released before it can rotate. Further details are now given on a few key fabrication processes: 1) through wafer etching; 2) precision DRIE; 3) multiwafer aligned fusion bonding; and 4) rotor release.
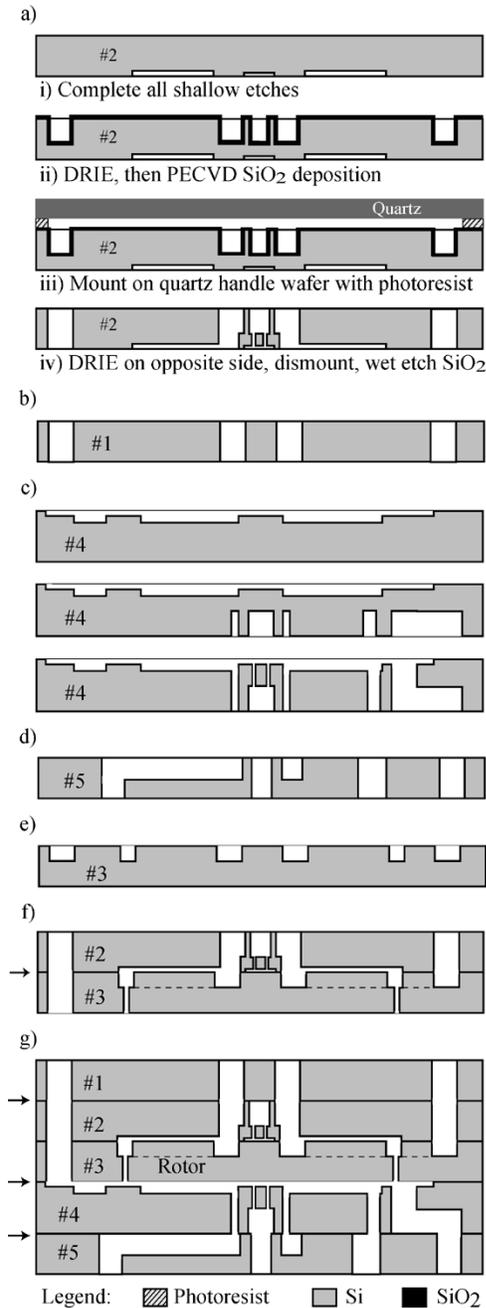
Fig. 7.    Process flow for the five wafer stack device. a) Forward end plate (wafer #2)—sample wafer process; b) forward foundation plate (wafer #1); c) aft end plate (wafer #4); d) aft foundation plate (wafer #5); e) rotor plate (wafer #3—w/o journal bearing gap etch); f) first bond (wafer #2 to #3), journal etch in wafer #3; g) triple bond to complete the five (5) wafer stack.

### B. Through Wafer Etching

During through etching, the wafers are temporarily mounted to a quartz substrate with photoresist to prevent leakage of He coolant when the etch breaks through the wafer [see Fig. 7(a)]. Before mounting, the bonding surface on the back side of wafers are protected with temporary PECVD oxide films to prevent contamination by hydrocarbon residue during the DRIE passivation step and damage from ion backscattering on the quartz handle wafer. For the die shown in Fig. 1, the back of the forward foundation plate (wafer #1) was not protected during the through etch from the aft side, hence, the resulting surface contamination

appears as dark regions around the holes. Such contamination would prevent adequate bonding if allowed on any bonding surface.

### C. DRIE of Critical Features

The required level of accuracy for the micromachined geometries is driven by their functionality. The two outermost wafers provide external fluidic and optical ports to the die, resulting in dimensions of the order of hundreds of microns without stringent precision requirements. Moving inward toward the rotor, the end plates (wafers #2 and #4) feature pressurized plenums (on their outer side) and 10 $\mu$m diameter by 100 $\mu$m long restrictors for the thrust bearings (on their side facing the rotor). Accurate restrictor diameter is critical since the axial stiffness of the thrust bearing depends on the pressure drop across the restrictor. Holes with a diameter of 10–11 $\mu$m were reproducibly achieved by exposing a 7-$\mu$m-diameter circle through a 6-$\mu$m-thick resist (AZ4620). The optimized process resulted in an 8–9-$\mu$m-diameter opening in the resist, and 1 $\mu$m of blowout in the silicon after 90 min of DRIE. Also critical is the journal bearing etch that cuts the rotor from the back of wafer #3 and consists of a high aspect ratio circumferential trench. From an initial 4-$\mu$m linewidth in the mask, a final silicon trench tapering from 17 to 9 $\mu$m wide and 300 $\mu$m deep was achieved in a 10-$\mu$m-thick AZ4620 photoresist after 4.5 h of DRIE (etch conditions: 105 sccm of $SF_6$ for 14 s active cycle, 0.5 s overlap, 12 W electrode power, and 800 W of coil power, followed by 40 sccm of $C_4F_8$ for 11 s active cycle, no overlap, 6 W electrode power and 600 W of coil power, and with the pressure control valve set at 65° and decreasing by 1.2° every 30 min). In both processes, the minimum feature size consistently achievable was limited by the tradeoff between the photoresist thickness necessary to withstand the etch duration, the reduced etch rate for narrow features, and the lower selectivity of DRIE recipes with less lateral etch. Higher anisotropy has been achieved for journal bearing etches by increasing the $SF_6$ flow rate by 2 sccm/h instead of changing the valve angle [20].

### D. Multi-Wafer Aligned Fusion Bonding

High yield fusion bonding is critical for the practical and economical viability of devices created from multiple bonded wafers. For the current device, multiple bonding sequences were investigated. Initially, individual wafers were incrementally bonded one at a time to the previous stack, repeating the cleaning, alignment, bonding, and annealing steps for every wafer. This approach increased the probability of surface contamination due to repeated high temperature annealing after each bond and the potential for residue to be trapped in the flow channels of multi-wafer stacks during the cleaning step. Instead, cleaning was limited to single wafers or bonded wafer pairs, which were all aligned and bonded before a final anneal. The final process therefore consisted of: 1) an RCA clean on wafers #1, #4, #5, and wafer pair #2-#3, finishing with 15 min in DI water to hydrolyze the surfaces; 2) inserting wafer #1 into the aligner (Electronic Vision EV 450) followed by wafer pair #2-#3; aligning and contacting; 3) re-inserting partial stack #1-#2-#3 into the aligner followed by wafer #4; aligning and contacting; 4) re-inserting partial wafer stack #1-#2-#3-#4
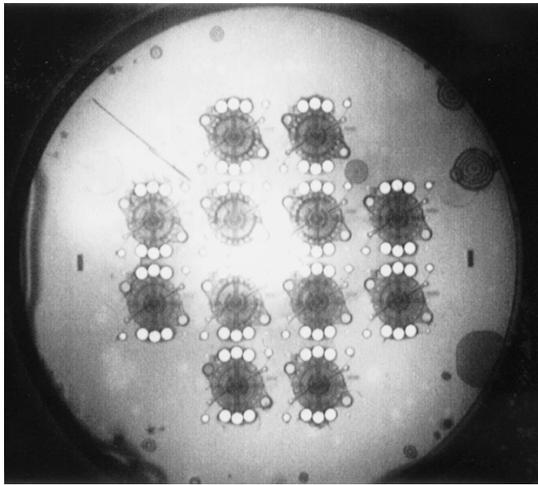
Fig. 8. Infrared photograph through a fusion bonded stack of five 100-mm-diameter wafers, illustrating successful bonding from the absence of dark fringes or spots over the device area.



(a) Schematic (side view)

(b) SEM before release     (c) SEM after release

Fig. 9. Schematic of the snap-off tab configuration and SEM of a snap-off tab before and after fracture.

followed by wafer #5; aligning and contacting; 5) bonding the complete wafer stack (Electronic Vision AB1-PV); 6) annealing the bonded wafer stack (1100 °C for 1 hr in $N_2$ ambient). Multiple wafer stacks were built using this approach with 90–100% bonding yield, based on the percentage of devices per wafer that do not delaminate nor exhibit leakage when pressurized. Infrared transmission through a typical bonded wafer stack is shown in Fig. 8, where poorly bonded areas (such as around the wafer periphery) appear as dark spots or fringes.

### E. Rotor Encapsulation and Release

A significant challenge in the fabrication of microrotors is to define a reliable process flow that creates free parts within enclosed structures or bearings, without tedious assembly and risk of damage. The approach adopted consists of bonding wafers #2 and #3 before etching the journal bearing gap, and creating silicon tabs that temporarily connect the rotor to the adjacent wafer (#2). As shown in Fig. 9(a), a silicon pillar extending from the rotor (wafer #3) joins to a horizontal beam on the forward end plate (wafer #2) when the wafers are fusion bonded. The journal bearing is then etched and the remaining three wafers are aligned fusion bonded to complete the five wafer stack, as described previously. An initial approach to release the rotor, demonstrated by Lin *et al.* [19], consisted of ablating the silicon tabs with laser assisted etching. This approach resulted in residue re-deposition and low yields. Here, the silicon links are mechanically fractured to release the rotor before testing, acting as *snap-off* tabs. The tab geometry was designed to provide a solid support against axial and in-plane motion of the rotor, while allowing a controlled failure mode when subjected to a lateral force. An array of configurations was designed using simple beam theory and stress concentration relations, and tested for a clean fracture at the roots of the pillar and beam [10]. Micromachined silicon needles were specially designed to reach down the main exhaust port (shown in Fig. 1) and apply the necessary lateral force to snap the tabs. Particles generated during snap-off were removed by flowing pressurized nitrogen through the main turbine flow path, out the main exhaust port. Fig. 9(b) and (c) shows such a snap-off tab structure before and after being fractured. The fractured
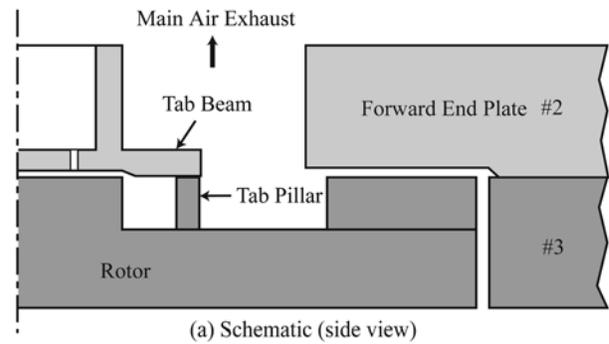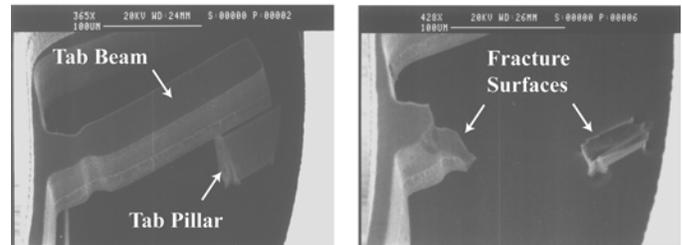
surfaces are raised from the disk surface and therefore reduce the potential for stress concentration. These snap-off tabs have been successfully used in all devices discussed next.

## IV. EXPERIMENTAL PROCEDURES AND RESULTS

### A. Packaging and Test Apparatus

To test the microturbine, multiple high-pressure fluidic connections must be established to the chip and optical access must be provided to the rotor for fiber optic speed measurement. The packaging approach consists of clamping the chip between acrylic plates to create sealed fluidic connections by pressing o-rings around the fluidic ports on both sides of the chip. These plates are machined with conduits that connect the o-rings to external tubulations, which are then connected to a gas handling system using Teflon tubing. The gas handling system controls six independent pressure supplies for (see Fig. 2): the turbine inlet, forward and aft thrust bearings, axial balance plenum, and two journal pressurization plenums. There is also a port for static pressure measurement between the rotor and stator blade rows, and two ambient exhaust ports for the main turbine air and aft thrust bearing. The pressurized fluidic ports are fed by a main high pressure nitrogen source, branching out to a pressure regulator, metering valve, mass flow meter, and pressure sensor for each of the six lines. The inlet nitrogen is filtered to 0.3 $\mu$m. PC-based buffered data acquisition collects the mass flow and pressure readings for real-time monitoring and postprocessing.

A hole in the top acrylic plate exposes the main exhaust port to the ambient and allows optical observation of the rotor. Speed is measured with a fiber optic sensor (Philtec Inc., model D6) that detects the passage of two diametrically opposite features on the silicon rotor. These two features, referred to as "speed bumps" in Fig. 3, are at the same height as the blades and the thrust bearing hub, and are located in the exhaust flow from the turbine. The fiber optic displacement measurement system is located above the
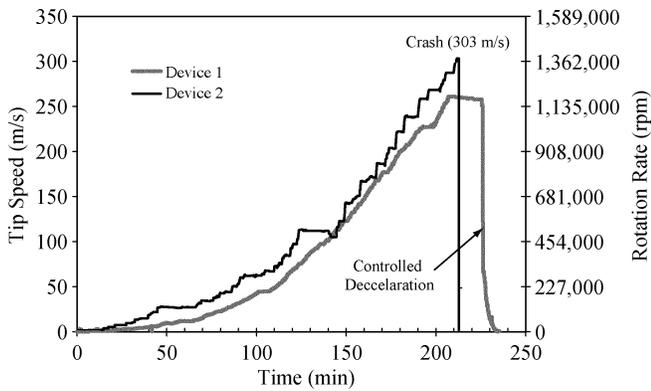
Fig. 10. Rotor speed as a function of time for two microturbine devices demonstrating the highest operating speed of over 300 m/s tip speed, or near 1.4 million rpm ($\pm0.5\%$ uncertainty).

speed bumps. With the rotor spinning, the output from this sensor approximates a low duty cycle square wave with frequency twice that of the rotor rotation rate. During operation, the signal from the speed sensor is monitored on a spectrum analyzer (HP 89 410A) to obtain the rotational speed and rotor vibrations.

### B. Testing Procedures

For proper operation, the rotor should be floating axially between the forward and aft thrust bearings. Optimal feed pressures that center the rotor are determined experimentally by fixing the pressure of one thrust bearing and varying the pressure of the opposite one. Since the flow resistance is an inverse function of the thrust bearing gap, the pressure versus flow rate response indicates the rotor axial position. The rotor travels from top most position down to the lowest position as the forward thrust bearing pressure is increased, while keeping the aft thrust bearing pressure fixed (see [10] and [19]).

Once axially positioned, rotation is accomplished by pressurizing the hydrostatic journal bearing to provide lateral support and the turbine inlet to apply torque to the rotor. These pressures are gradually raised according to a predetermined schedule in order to maintain stable journal bearing operation as the rotational speed increases. Spectral content of the optical sensor is used to measure speed and assess rotor stability.

### C. High-Speed Results

Fig. 10 shows the rotation rate of two devices as they are slowly accelerated in a stable manner. Device 1 was brought up to a tip speed of 260 m/s (1.2 million rpm) and was held there for 20 min (a pressure leak resulted in a slight deceleration). The rotor was then rapidly decelerated to stop. Device 2 reached a tip speed of 303 m/s (1.4 million rpm) prior to going unstable, crashing, and fracturing into many pieces. Both devices achieved on the order of $10^8$ revolutions.

The turbine operating line is shown in Fig. 11 for five different devices, taken from three different completed wafer stacks. Also shown in this figure are data points calculated using MISES with the corresponding mechanical power delivered by the microturbine. These predicted operating points were determined by varying the turbine inlet pressure at a given speed in order to match the turbine power with the viscous power. Fully developed Couette flow in the journal bearing, thrust bearings, and rotor back side are assumed, as well as ambient temperature
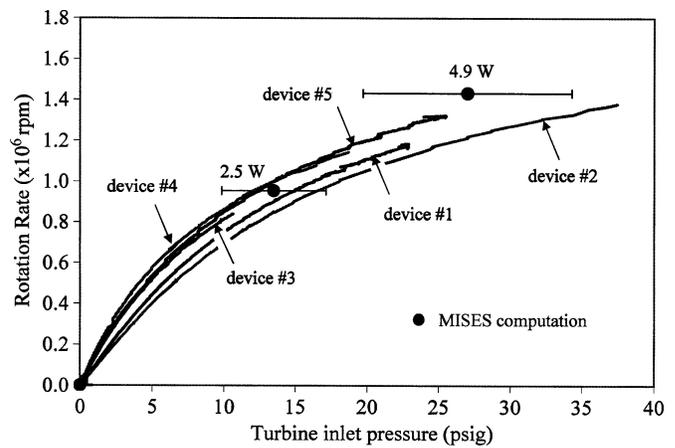


Fig. 11. Rotation rate as a function of turbine inlet pressure for five different devices along with predicted values (MISES), showing repeatability and qualitative agreement with expected performance ($\pm0.8$ psi uncertainty in measured pressure and $\pm0.5\%$ on speed).
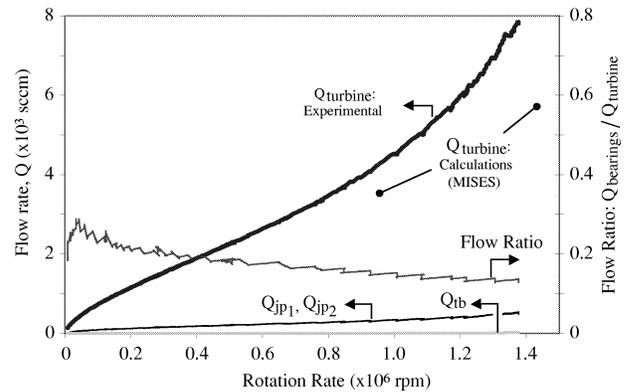


Fig. 12. Turbine and bearing flow rates over the range of operating speeds for Device 2. Uncertainty in the main flow is $\pm200$ sccm, in the journal pressurization plenums (jp1 & jp2) is $\pm50$ sccm, and in the thrust bearings (tb) is $\pm0.5$ sccm.

turbine inlet air. At 1.4 million rpm, the microturbine is predicted to deliver nearly 5 W of mechanical power with a torque over 30 $\mu N - m$. The computational results are dependent on the axial position of the rotor, which affects the amount of drag. The uncertainty bars on the MISES data points are associated with an expected $\pm0.5$ $\mu m$ uncertainty in the axial position of the rotor. The MISES results do not compensate for the decrease in mass flow due to blockage from boundary layer growth on the end-walls (3-D effect), which likely explains why the actual device required a somewhat higher turbine pressure for a given speed to generate sufficient torque.

### D. Microbearing System Operation

The mass flow rates supplied to Device 2 are shown in Fig. 12. Here the experimental turbine flow rate ($Q_{main}$) is somewhat higher than predicted in MISES, due to the increased pressure required to operate the turbine. The flow rates supplied to each journal pressurization plenum ($Q_{jp1}$ and $Q_{jp2}$) are essentially equal, lying on top of each other in Fig. 12. The thrust balance plenum was sealed with negligible leakage. Also shown in Fig. 12 is an aggregate of the bearing flows normalized by the main turbine flow. This ratio peaks at 30% at low speed, decreases to 13% at the highest speed achieved and trends downwards for higher speeds. Thus, for high-speed applications, the
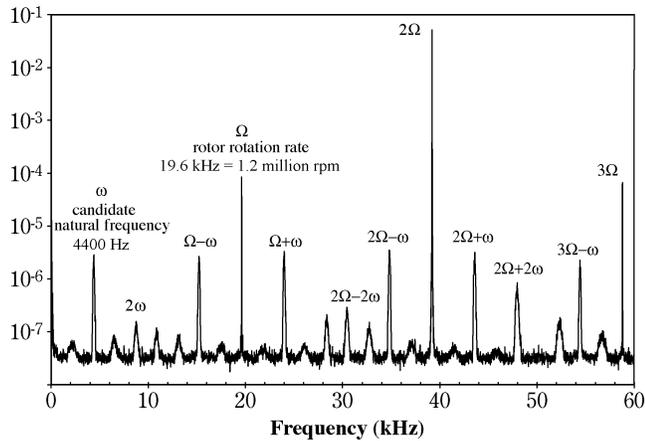
Fig. 13. Power spectrum of the optical speed sensor signal showing the speed bump frequency ($2\,\Omega$) and the rotor rotation rate ($\Omega$), as well as other peaks corresponding to the natural frequency ($\omega$) and its combinations with the rotation frequency.

flow needed to operate the bearing system is small compared to the main turbine flow. At 1.4 million rpm, the differential pressure across the journal bearing was about 5 psi, which is significantly less than the turbine inlet pressure.

The thrust bearings proved sufficiently stiff so as not to require much manipulation during a run. For Device 2, the back side thrust bearing ran with a constant supply pressure of 35 psig while the front side thrust bearing was varied from about 60 to 85 psig. Each thrust bearing required about 10 sccm of nitrogen, which is negligible in the scale of the other flow rates. For practical applications, the thrust bearings should be redesigned to operate at feed pressures less than the turbine inlet pressure over the entire speed range or be replaced with hydrodynamic thrust bearings.

## V. DISCUSSIONS

### A. Journal Bearing Stability and Monitoring

A key element at achieving high speed operation was the real-time control of the journal bearing pressure, using the spectrum analyzer to monitor rotor stability. The spectrum content of the optical sensor shows a strong peak at twice the rotation rate (two speed bumps per rotation), at the rotation rate (due to fabrication asymmetry), and also at higher harmonics. Additional peaks also appear when the journal bearing is excited at its natural frequency, as shown in Fig. 13. As mentioned earlier, the hydrostatic journal bearing can be viewed as a damped spring that supports the rotor, and as such has a natural frequency associated with it. Whirling of the rotor at the natural frequency of the bearing results in precession of the speed bumps; this appears as a pulsewidth modulation of the signal at the whirl frequency, which is captured in the spectral analysis. The measured interaction between the rotation rate and the bearing natural frequency also results in peaks at their combinations, identified in Fig. 13. Operation has shown that appearance of these extra peaks is associated with the approach of a stability boundary. When these peaks appear, the differential pressure across the journal bearing is adjusted to change the natural frequency, which prevents resonance, stabilizes the rotor, and make these peaks vanish. An initial journal bearing pressurization schedule was determined

experimentally through this approach, then used on subsequent runs. It was found that maintaining a constant ratio of rotational speed to journal bearing differential pressure, $\Omega/(\Delta P)^n$, consistently allowed high speed operation (500 000 rpm or more) by operating the rotor between the first and second journal bearing natural frequencies. The schedule consisted of maintaining: $(\Omega/\Omega_{\text{ref}})/(\Delta P/P_o)^{0.83} = 0.12$ for an axial differential pressure below 1 psi and $(\Omega/\Omega_{\text{ref}})/(\Delta P/P_o)^2 = 4.5$ above 1 psi, where rotational speed is nondimensionalized by $\Omega_{\text{ref}} = 2.4 \times 10^6$ rpm and the pressure differential is nondimensionalized by atmospheric pressure ($P_o$). Further discussion of the rotor dynamic behavior described here can be found elsewhere [25].

### B. Failure Mechanisms

Two modes of failure have been observed: 1) low-speed journal bearing failure; and 2) high-speed fatal crashes. For multiple devices, rotation rate was limited to low speeds on the order of 60 000 rpm, beyond which solid contact in the journal bearing, or grinding, was experienced. Relatively high journal pressure differentials were required (up to 5 psi) to reach this speed compared to successful high-speed devices, suggesting limitations from the journal bearing operation. Devices that operate well beyond this speed typically fail catastrophically at high speeds (over 1 million rpm), such as Device 1 discussed previously in Section IV.

The main failure mechanism in both scenarios is suggested to be the inability of the journal bearing to withstand loads induced by rotor imbalance. Imbalance results from misalignment of the journal bearing geometric center to the rotor's center of mass, such as from misalignment of the front and back side masks of the rotor plate (wafer #3), and depth nonuniformity of the blade DRIE across the rotor. When the rotor operates at rotation rates higher than the journal bearing natural frequency (i.e., supercritically), as it does through most of its operating range, the rotor spins around its center of mass rather than its geometric center [23]. For devices limited to low speed operation, it is expected that the imbalance is sufficient to force the rotor into solid contact when the rotor is accelerated through the bearing natural frequency. Even for rotors with small imbalance, a slight offset of the rotor produces circumferential pumping of fluid, and causes the development of hydrodynamic forces in the journal bearing gap. These hydrodynamic forces tend to be destabilizing [24] and increase with the square of speed. Rotors that have achieved high speed operation are, therefore, expected to be sufficiently well balanced to transition into supercritical operation, but remain limited to an upper threshold speed that depends on the level of imbalance and the journal bearing design.

Traditionally, rotating machinery is actively balanced before high speed operation [14]. For microfabricated rotors, such balancing techniques have not yet been developed. Our current microfabrication techniques appear to be sufficiently accurate to yield adequately balanced rotors, as confirmed by the high-speed results presented herein. The level of geometric control is however marginal, since only a few rotors from each completed wafer stack have successfully achieved high speeds.

Ultimately, rotor speed should be limited by the mechanical failure of the structure under centrifugal loads, which depends on the geometric design and material properties. Single-crystal

silicon offers high strength-to-density ratio $(\sigma_u/\rho)$ compared to typical materials used for high-speed turbomachinery, and thus the simple rotor geometry adopted here (plane disk with cantilevered blades) is expected to withstand tip speeds beyond 500 m/s [26]. Since imperfections introduced during rotor etching or release may have created unexpected stress concentration, structural failure cannot be ruled out for high-speed rotors tested herein. Further analysis and experimental characterization on the specific microfabricated rotors is required in order to determine the probability of structural failure.

### C. Power Density

At the tip speeds achieved, these microfabricated rotors have demonstrated unprecedented levels of power density. Results presented herein suggest a ratio of mechanical power to turbomachinery volume of over $4\,\mathrm{W/mm}^3$, which is more than twice that achieved by modern aircraft engine technology. Based on microturbine aerodynamic calculations using the MISES CFD code validated herein, silicon microturbines could be designed with an order of magnitude higher power density. This dramatic difference with macroscale machinery is a direct consequence of scaling laws. Micro gas turbine engines and other turbomachinery-based microsystems can be expected to operate with similar pressure ratios as their large scale counterparts, when operated at similar peripheral speeds. The microturbine however achieves this pressure ratio over a shorter distance than conventional turbines, which is set by the scale of the blades. The same power per unit flow rate, or inlet area, is therefore achieved but over a shorter length. This reduction in length, and consequently volume, provides the dramatic increase in power density. This same principle would also apply to other fluid machinery, since power typically scales as the flow area, i.e., proportional to $L^2$ where $L$ a characteristic length dimension, while the volume scales as $L^3$. Power density, therefore, scales as $1/L$ and tends to increases at smaller scales. This benefit is however attenuated by a reduction in efficiency in fluid machinery due to typically lower Reynolds numbers, higher viscous drag, and higher heat transfer rates in microsystems [16].

## VI. CONCLUSION

Silicon microturbine rotors supported on gas lubricated bearings have been spun in a sustained manner at high speeds. These devices have operated at tip speeds two orders of magnitude greater than previously demonstrated with MEMS technology, and are among the highest rotational speed machines made by man, with near 1.4 million revolutions per minute.

The use of microfabrication techniques, such as lithographic patterning, DRIE of silicon, and aligned fusion wafer bonding were central to this realization. Since the rotors were fabricated from single-crystal silicon bulk substrates, they could withstand high mechanical stresses induced by centrifugal forces, even with the simple rotor design imposed by the 2-D nature of lithography-based MEMS fabrication techniques. This approach has shown the ability to provide well balanced rotors *as-fabricated*, although tighter tolerances or tailored balancing approaches are desirable.

Two key technologies for micro heat engines have been demonstrated: microturbomachinery and microfabricated gas

bearings. A radial inflow, constant blade height, single-stage planar turbine was shown to operate as predicted by computational fluid dynamics, providing near 5 W of mechanical power for a 4.2-mm diameter rotor operating at 303 m/s tip speed. Microfabricated, hydrostatic gas-lubricated thrust bearings and journal bearings were also demonstrated to be capable of high-speed operation. Particularly, a novel hydrostatic principle was implemented for the journal bearings, which are shorter and have larger clearances than conventional designs.

We are currently trying to understand more fully the stability characteristics of micro gas bearings, with the goal of establishing a microbearing design basis for implementation in practical systems. For example, self-sustained hydrodynamic thrust bearings have already been demonstrated [27]. The fabrication efforts are focused on improving alignment precision and etch uniformity, to decrease the rotor imbalance. We believe this technology will serve as a building block for a wide array of high-power density MEMS devices based on rotating components, including pumps, compressors, and heat engines. These will enable the use of power MEMS for applications such as portable power generation, micropropulsion of micro air vehicles and rockets, microfluidic pumping, as well as cooling of microelectronics, sensors, and people.

## REFERENCES

[1] M. Mehregany, P. Nagakar, S. D. Senturia, and J. H. Lang, "Operation of microfabricated harmonic and ordinary side-drive motors," in *Proc. IEEE Micro Electro Mech. Syst.*, Napa Valley, CA, Feb. 12–14, 1990.

[2] L. Fan, Y. Tai, and R. Muller, "IC-processed electrostatic micromotors," *Sens. Actuators*, vol. 20, pp. 41–47, 1989.

[3] H. Guckel, T. Christenson, K. Skrobis, T. Jung, J. Klein, K. Hartojo, and I. Widjaja, "A first functional current excited planar rotational magnetic micromotor," in *Proc. IEEE Micro Electro Mech. Syst.*, Fort Lauderdale, FL, Feb. 1993.

[4] U. Wallrabe, P. Bley, B. Krevet, W. Menz, and J. Mohr, "Design rules and test of electrostatic micromotors made by the LIGA process," *J. Micromech. Microeng.*, vol. 4, pp. 40–45, 1994.

[5] J. J. Sniegowski, S. L. Miller, G. F. LaVigne, M. S. Rodgers, and P. J. McWhorter, "Monolithic geared-mechanisms driven by a polysilicon surface-micromachined on-chip electrostatic microengine," in *Proc. Solid-State Sens. Actuators Workshop*, Hilton Head Island, SC, Jun. 2–6, 1996, pp. 178–182.

[6] S. L. Miller, G. LaVigne, M. S. Rodgers, J. J. Sniegowski, J. P. Waters, and P. J. McWhorter, "Routes to failure in rotating MEMS devices experiences sliding friction," in *Proc. SPIE Micromachined Devices and Components III*, vol. 3224, Austin, TX, Sep. 29–30, 1997, pp. 24–30.

[7] A. H. Epstein *et al.*, "Micro-heat engine, gas turbine, and rocket engines—the MIT microengine project," presented at the *28th AIAA Fluid Dynamics Conf.*, Snowmass Village, CO, June 1997, Paper 97-1773.

[8] A. H. Epstein, S. A. Jacobson, J. Protz, and L. G. Fréchette, "Shirtbutton-sized gas turbines: the engineering challenges of micro high-speed rotating machinery," in *Proc. 8th Int. Symp. Transport Phenomena and Dynamics of Rotating Machinery*, Honolulu, HI, Jan. 2000.

[9] A. P. London, A. H. Epstein, and J. L. Kerrebrock, "High-pressure bipropellant microrocket engine," *AIAA J. Propulsion and Power*, vol. 17, no. 4, pp. 780–787, Jul. 2001.

[10] L. G. Fréchette, "Development of a microfabricated silicon motor-driven compression system," Ph.D. dissertation, Dept. Aero. Astro., Mass. Inst. Technol., Cambridge, 2000.

[11] I. A. Waitz, G. Gauba, and Y.-S. Tzeng, "Combustors for micro-gas turbine engines," *ASME J. Fluids Eng.*, vol. 20, pp. 109–117, 1998.

[12] A. Mehra, X. Zhang, A. A. Ayón, I. A. Waitz, M. A. Schmidt, and C. Spadaccini, "A six-wafer combustion system for a silicon micro gas turbine engine," *J. Microelectromech. Syst.*, vol. 9, no. 4, pp. 517–527, Dec. 2000.

[13] E. S. Piekos and K. S. Breuer, "Pseudo-spectral orbit simulation of nonideal gas-lubricated journal bearings for microfabricated turbomachines," *ASME J. Tribol.*, vol. 121, pp. 604–609, Jul. 1999.

[14] D. J. Orr, "Macro-scale investigation of high-speed gas bearings for MEMS devices," Ph.D. dissertation, Dept. Aero. Astro., Mass. Inst. Technol., 1999.

[15] A. Mehra, "Computational investigation and design of low reynolds number micro-turbomachinery," S.M. thesis, Dept. Aero. Astro., Mass. Inst. Technol., Cambridge, 1997.

[16] S. A. Jacobson, "Aerothermal challenges in the design of a microfabricated gas turbine engine," presented at the 29th Fluid Dynamics Conf., Albuquerque, NM, Jun. 1998, paper 98-2445.

[17] S. F. Nagle, "An electric induction micromotor," *J. Microelectromech. Syst.*.

[18] L. G. Fréchette, S. N. Nagle, R. Ghodssi, S. D. Umans, M. A. Schmidt, and J. H. Lang, "An electrostatic induction micromotor supported on gas-lubricated bearings," in *Proc. 14th IEEE Int. Micro Electro Mech. Syst.*, Interlaken, Switzerland, Jan. 2001.

[19] C.-C. Lin, R. Ghodssi, A. A. Ayón, D. Z. Chen, S. A. Jacobson, K. S. Breuer, A. H. Epstein, and M. A. Schmidt, "Fabrication and characterization of a micro turbine/bearing rig," in *Proc. IEEE Microelectromech. Syst.*, Orlando, FL, Jan. 1999.

[20] A. A. Ayón, X. Zhang, and R. Khanna, "Ultra deep anisotropic silicon trenches using deep reactive ion etching," in *Proc. Solid-State Sensor and Actuator Workshop*, Hilton Head Island, SC, Jun. 4–8, 2000.

[21] L. G. Fréchette, S. A. Jacobson, F. F. Ehrich, R. Ghodssi, R. Khanna, C. W. Wong, X. Zhang, K. S. Breuer, M. A. Schmidt, and A. H. Epstein, "Demonstration of a microfabricated high-speed turbine supported on gas bearings," in *Proc. Solid-State Sens. Actuator Workshop*, Hilton Head Island, SC, Jun. 4–8, 2000.

[22] M. Drela and H. Youngren, MISES 2.1, MIT Computational Aerospace Sciences Lab., Cambridge, Jun. 1995.

[23] D. Childs, *Turbomachinery Rotordynamics*. New York: Wiley, 1993.

[24] K. S. Breuer, "Lubrication in MEMS," in *CRC Handbook on MEMS*, M. Gad-el-Hak, Ed. Boca Raton, FL: CRC, 2002.

[25] F. F. Ehrich and S. A. Jacobson, "Development of high-speed gas bearings for high-power density microdevices," *ASME J. Eng. Gas*, vol. 125, pp. 141–148, Jan. 2003.

[26] K.-S. Chen, S. M. Spearing, and N. N. Nemeth, "Structural design of a silicon micro-turbo generator," *AIAA J.*, vol. 39, no. 4, pp. 720–728, 2001.

[27] C. W. Wong, X. Zhang, S. A. Jacobson, and A. H. Epstein, "A self-acting thrust bearing for high-speed microrotors," in *Proc. 15th IEEE Int. Micro Electro Mech. Syst.*, Las Vegas, NV, Jan. 20–24, 2002.

**Stuart A. Jacobson** received the B.S.E. degree from Princeton University, Princeton, NJ, in 1986, and the M.S. and Ph.D. degrees from Stanford University, Stanford, CA, in 1989 and 1995, respectively.

He is currently a Research Engineer with the Gas Turbine Laboratory, Massachusetts Institute of Technology (MIT), Cambridge. In this position, he serves as the Deputy Director of the MIT Microengine Project, overseeing research on microfabricated gas turbine generators and rocket engines. His current research interests include portable power generation, power MEMS, small-scale propulsion, microfluidics, and high-speed microbearings.

Dr. Jacobson is a Member of the American Society of Mechanical Engineers (ASME).

**Kenneth S. Breuer** received the Ph.D. degree from the Massachusetts Institute of Technology (MIT), Cambridge, in 1988.

From 1990 to 1999, he was with the Department of Aeronautics and Astronautics, MIT, before moving to Brown University, where he is currently Professor of engineering. His research interests are in the fluid mechanics of micron and nanometer scale systems.

Dr. Breuer is a Senior Member of the American Society of Mechanical Engineers (ASME).

**Fredric F. Ehrich** received the S.B., M.E., and Sc.D. degrees in mechanical engineering from the Massachusetts Institute of Technology, Cambridge, in 1947, 1950, and 1951, respectively.

He spent the 1947–1948 academic year with Delft Technical University, the Netherlands. His entire professional career has been dedicated to aircraft gas turbine technology with particular focus on rotordynamics. From 1951 to 1957, he worked for the Westinghouse Aircraft Gas Turbine Division, Philadelphia, PA, and Kansas City, MO, in engineering and engineering leadership positions in research, analysis, design, and development. As part of his duties, he spent 1955 to 1956 as Westinghouse's technical representative at Rolls Royce Aero Engines, Derby, U.K. Since 1957, he was associated with GE's Aircraft Engine activity in Lynn, MA, in Senior Engineering and Engineering Leadership positions in gas turbine technology research and component and engine design and development. He retired from GE in January 1994 and is still active in consulting and in teaching and research on the gas bearings and rotordynamics of the MIT/GTL Micro-engine and as a Senior Lecturer at MIT. He is the author of more than 45 published technical papers, principally in the field of rotordynamics of high-speed rotating machinery. He is the Editor-in-Chief of and a principal contributor to the *Handbook of Rotordynamics* (New York: McGraw-Hill, 1991) and in a revised edition (Melbourne, Australia: Krieger, 1999).

Dr. Ehrich was elected to the academic honorary societies Tau Beta Pi, Pi Tau Sigma, and Sigma Xi and was elected to membership in the National Academy of Engineering in 1992. He is a Fellow of the American Society of Mechanical Engineers (ASME). In 1995, he was inducted into the GE Propulsion Hall of Fame.

**Luc G. Fréchette** (M'01) received the Ph.D. degree from the Massachusetts Institute of Technology (MIT), Cambridge, in 2000.

He is currently the Canada Research Chair in Power MEMS and an Assistant Professor of mechanical engineering at the Université de Sherbrooke, Québec, Canada. From 2000 to 2004, he was an Assistant Professor of mechanical engineering at Columbia University, NY. His research interests are in microengineering of miniature systems for energy conversion (Power MEMS), such as microfabricated heat engines and fuel cells, with activities ranging from integrated device development to fundamental microfluidics, heat and mass transfer studies in such microsystems. He also enjoys developing MEMS sensors and actuators for aerospace applications.

Dr. Fréchette is a Member of the American Society of Mechanical Engineers (ASME) and the AIAA society.

**Reza Ghodssi** (S'92–M'97) was born in Tehran, Iran, in 1966. He received the B.S., M.S., and Ph.D. degrees in electrical engineering from the University of Wisconsin at Madison, in 1990, 1992, and 1996, respectively. His Ph.D. dissertation was focused on development of a high aspect ratio microfabrication process for an electrostatic driven MEMS device using X-ray lithography and LIGA technology.

He was a Postdoctoral Associate and a Research Scientist with the Microsystems Technology Laboratories and the Gas Turbine Laboratory, Massachusetts Institute of Technology (MIT), Cambridge, from 1997 until 1999. During his tenure at MIT, he developed the building block MEMS fabrication technologies for a microturbine generator device and also served as an Assistant Director on that project. In January 2000, he joined the Department of Electrical and Computer Engineering and the Institute for Systems Research, University of Maryland (UMD), College Park, as an Assistant Professor. His research interests are in design and development of microfabrication technologies and their applications to microsensors, microactuators and integrative microsystems.

Dr. Ghodssi was awarded the 2001 UMD George Corcoran Award, 2002 National Science Foundation CAREER Award, and the 2003 UMD Outstanding Systems Engineering Faculty Award. He has served as a program Co-Chairman for the 2001 International Semiconductor Device Research Symposium (ISDRS) and, since 2002, as a Chairman of the MEMS and NEMS Technical Group at the American Vacuum Society (AVS). He is a cofounder of the MEMS Alliance Group in the greater Washington area and a member of the AVS and MRS societies.

**Ravi Khanna** (M'86) received the B.S. degree in physics in 1983 and the M.S. and Ph.D. degrees in electrical engineering from the Pennsylvania State University, University Park, in 1992.

From 1992 to 1998, he was a Senior Device and Process Engineer at Skyworks Solutions, Woburn, MA, where he oversaw the design, fabrication, and testing of microwave semiconductor components. From 1998 to 2004, he enjoyed the challenges of MEMS process development and implementation on the MIT Micro-Engine and MicroRocket programs.

**Chee Wei Wong** (M'03) received the B.S. (highest honors) and B.A. (highest honors) degrees in mechanical engineering and economics, respectively, from the University of California, Berkeley, in 1999, and the M.S. and Sc.D. degrees from the Massachusetts Institute of Technology (MIT), Cambridge, in 2001 and 2003, respectively.

He is currently an Assistant Professor with the Department of Mechanical Engineering, Columbia University, New York, NY. He was a Postdoctoral Associate briefly at the MIT Microphotonics Center in 2003. He enjoys working on micro- and nanoscale phenomena in general; specifically, on photonic crystal nanostructures, photonic microcavities, NEMS/MEMS, high-density photonic integrated circuits, and derived biological applications with optics.

Dr. Wong is a Member of American Physics Society (APS), the American Society of Mechanical Engineers (ASME), the Optical Society of America (OSA), and Sigma Xi.

**Xin Zhang** (M'00) received the Ph.D. degree in mechanical engineering from Hong Kong University of Science and Technology, Hong Kong, in 1998.

She is an Assistant Professor with the Department of Manufacturing Engineering and the Department of Aerospace and Mechanical Engineering, Boston University, Boston, MA. She also holds a Fraunhofer professorship through association and collaboration with the Fraunhofer USA Center for Manufacturing Innovation. From 1998 to 2001, she was a Research Scientist with the Massachusetts Institute of Technology (MIT), Cambridge, where she had worked at the MIT MicroEngine project. Currently, she leads the Laboratory for Microsystems Technology (LMST), Boston University, to perform research on MEMS and NEMS. Specifically, she is interested in applying materials science, micro/nanomechanics, and micro/nanomanufacturing technologies to solve various engineering problems that are motivated by practical applications in MEMS/NEMS and emerging bionanotechnologies.

Dr. Zhang is the recipient of SPRInG Award at Boston University (2002–2003) and the NSF CAREER Award (2003–2008). She is a Member of the American Society of Mechanical Engineers (ASME).

**Martin A. Schmidt** (S'88–M'85–SM'00–F'03) received the B.S. degree in electrical and computer engineering from Rensselaer Polytechnic Institute, Troy, NY, in 1981 and the S.M. and Ph.D. degrees in electrical engineering and computer science from the Massachusetts Institute of Technology (MIT), Cambridge, in 1983 and 1988, respectively.

He is an expert in microelectromechanical systems, devices with miniature moving parts made with fabrication techniques of microelectronics. He investigates microfabrication technologies for integrated circuits, sensors, and actuators; design of micromechanical sensor and actuator systems; mechanical properties of microelectronic materials, with emphasis on silicon wafer bonding technology; integrated microsensors; and microfluidic devices. His current research projects involve novel applications of MEMS technologies to a variety of fields, including miniature gas turbines, miniature chemical reactors, microswitches, biological applications and sensors monolithically integrated with electronics. His work has been sponsored by NSF, ARO, SRC, AFOSR, and a host of industries. He has more than 130 refereed technical publications and 28 patents.

Dr. Schmidt is a recipient of a number of awards including the Ruth and Joel Spira Teaching Award, the NSF Presidential Young Investigator Award, and an honorary doctorate from the Technical University of Denmark.

**Alan H. Epstein** received the S.B., S.M., and Ph.D. degrees in aeronautics and astronautics from the Massachusetts Institute of Technology (MIT), Cambridge.

He is the R.C. Maclaurin Professor of Aeronautics and Astronautics and Director of the Gas Turbine Laboratory, MIT, where he also teaches and does research in the fields of energy conversion, aero and rocket propulsion, and microsystems—specifically micropropulsion and energy conversion devices.

Dr. Epstein is a Member of American Society of Mechanical Engineers (ASME), a Fellow of the AIAA, and a Member of the National Academy of Engineering.